Seismic attribute detection of faults and fluid pathways within an active strike-slip shear zone: New insights from high-resolution 3D P-Cable™ seismic data along the Hosgri Fault, offshore California

Jared W. Kluesner[1] and Daniel S. Brothers[1]

Abstract

Poststack data conditioning and neural-network seismic attribute workflows are used to detect and visualize faulting and fluid migration pathways within a 13.7 km^2 3D P-Cable™ seismic volume located along the Hosgri Fault Zone offshore central California. The high-resolution 3D volume used in this study was collected in 2012 as part of Pacific Gas and Electric's Central California Seismic Imaging Project. Three-dimensional seismic reflection data were acquired using a triple-plate boomer source (1.75 kJ) and a short-offset, 14-streamer, P-Cable system. The high-resolution seismic data were processed into a prestack time-migrated 3D volume and publically released in 2014. Postprocessing, we employed dip-steering (dip and azimuth) and structural filtering to enhance laterally continuous events and remove random noise and acquisition artifacts. In addition, the structural filtering was used to enhance laterally continuous edges, such as faults. Following data conditioning, neural-network based meta-attribute workflows were used to detect and visualize faults and probable fluid-migration pathways within the 3D seismic volume. The workflow used in this study clearly illustrates the utility of advanced attribute analysis applied to high-resolution 3D P-Cable data. For example, results from the fault attribute workflow reveal a network of splayed and convergent fault strands within an approximately 1.3 km wide shear zone that is characterized by distinctive sections of transpressional and transtensional dominance. Neural-network chimney attribute calculations indicate that fluids are concentrated along discrete faults in the transtensional zones, but appear to be more broadly distributed amongst fault bounded anticlines and structurally controlled traps in the transpressional zones. These results provide high-resolution, 3D constraints on the relationships between strike-slip fault mechanics, substrate deformation, and fluid migration along an active fault system offshore central California.

Introduction

Seismic attribute calculations are considered to be essential steps in 3D seismic interpretation workflows employed by the petroleum exploration industry. The results can accelerate, and in many cases, provide quantitative justification for the interpretation of a variety of geologic features. Nevertheless, academic researchers aiming to understand near-surface processes and offshore hazards (e.g., by active tectonics and slope stability studies) rarely have access to high-resolution 3D seismic data. Thus, the application of seismic attribute workflows to such problems and data remains largely unexplored. New 3D seismic technology, such as the high-resolution P-Cable™ system (e.g., Brookshire and Scott, 2015), and expanded access to publically available 3D data sets are providing opportunities to develop advanced 3D seismic attribute workflows to better understand the near-surface processes and improve hazard assessments.

Over the past 20 years, a number of well-known seismic attributes have been developed for the analysis of seismic discontinuities related to geologic structures. This includes attributes such as coherency (Bahorich and Farmer, 1995; Marfurt et al., 1998, 1999), similarity (Tingdahl, 1999; Tingdahl et al., 2001; Tingdahl and de Rooij, 2005), volumetric curvature (Roberts, 2001; Al-Dossary and Marfurt, 2006; Chopra and Marfurt, 2010), and other geometric attributes that perform mathematic calculations between various lateral trace segments and across defined time gates (e.g., Chopra and Marfurt, 2005, 2007). Standard seismic discontinuity attribute calculations without structural information, such as coherency and similarity, are frequently equated to fault-attribute calculations. However, both approaches may struggle to differentiate between geologic features, such as faults, erosional incisions, gas chimneys, steeply dipping strata, karst collapse struc-

[1]Pacific Coastal and Marine Science Center, U.S. Geological Survey, Santa Cruz, California, USA. E-mail: jkluesner@usgs.gov; dbrothers@usgs.gov.

Manuscript received by the Editor 11 August 2015; revised manuscript received 9 October 2015; published online 15 February 2016. This paper appears in *Interpretation*, Vol. 4, No. 1 (February 2016); p. SB131–SB148, 11 FIGS., 2 TABLES.

http://dx.doi.org/10.1190/INT-2015-0143.1. Society of Exploration Geophysicists and American Association of Petroleum Geologists

tures, and also data artifacts. Detection and isolation of a desired geologic target can be improved by combining structurally orientated calculations with discontinuity attribute calculations (e.g., Gersztenkorn and Marfurt, 1999; Marfurt et al., 1999; Tingdahl, 1999; Tingdahl et al., 2001; Tingdahl and de Groot, 2003). Yet, undesirable seismic discontinuities (e.g., data artifacts) can still be present, possibly complicating the calculated attribute result and potentially confusing the interpreter (Marfurt and Alves, 2014).

In an effort to better detect geologic targets and isolate their signals from nondesired geologic features and/or data artifacts, the combination of multiple attributes, or parameterizations of attributes, has been shown to provide substantial benefit to the seismic interpreter. This multiattribute approach was developed using crossplotting techniques (Chopra and Marfurt, 2009) and soft computing neural-network methodology (Russell et al., 1997; Meldahl et al., 1999, 2001; Aminzadeh and de Groot, 2004, 2006; Tingdahl and de Rooij, 2005). The artificial neural-network approach, also referred to as multiattribute cluster analysis (Marfurt, 2014), uses multiple weighted seismic attributes and can be supervised and trained by the interpreter to provide optimized detection of targeted geologic features. The approach includes the detection and isolation of geologic features that produce particular changes in the seismic response, including faults (Tingdahl and de Rooij, 2005; Brouwer and Huck, 2011), gas chimneys (Heggland, 2005; Ligtenberg, 2005; Connolly and Garcia, 2012; Kluesner et al., 2013; Brothers et al., 2014; Connolly, 2015), salt bodies (Aminzadeh and de Groot, 2005), and various lithofacies (Ohl and Raef, 2014). If appropriately developed, parameterized, and optimized, the combination of multiple attributes into "meta-attributes" can produce results with greater contrast and fewer unwanted signals than individual attributes (e.g., Tingdahl and de Rooij, 2005; Mirkamali et al., 2013). Furthermore, several attributes can be visually blended for multiattribute display, providing visual enhancement for a more informed interpretation of the seismic data (Marfurt, 2015).

In this study, we use a neural-network multiattribute approach in an attempt to optimize the detection and visualization of faults and fluid pathways within a tectonically active strike-slip shear zone. The high-resolution 3D seismic data volume used in this study was collected in shallow water across a portion of the Hosgri Fault Zone (HFZ), located offshore central California (PG&E, 2014). Seismic acquisition was carried out using the P-Cable system, a 3D seismic acquisition system used to bridge the resolution gap between traditional 2D/3D seismic reflection operations and high-resolution subbottom acoustic data (e.g., Petersen et al., 2010; Nishenko et al., 2012; Ebuna et al., 2013; Brookshire and Scott, 2015). High-frequency noise, possibly from surface statics or navigation errors, is present throughout the publicly released 3D volume. This high-frequency noise limits the accuracy and quality of seismic attribute calculations. To suppress the unwanted noise, we apply a data conditioning workflow that consists of structural directionality calculations and structural filters. The filtered data are then input into attribute calculations, including maximum curvature and two supervised neural-network meta-attribute workflows tailored to detect probable faults and chimneys within the 3D volume. The meta-attribute results show significant noise tolerance and improvement over single discontinuity attribute calculations.

Last, the results from this study provide high-resolution 3D constraints on the relationship between faulting, deformation, and apparent fluid migration within an active strike-slip fault system. The neural-network fault attribute results provide 3D delineation of the geometry and internal structure of restraining and releasing bends, step-over zones, convergence zones, and paired fault bends (PFBs). Analysis of the neural-network chimney attribute suggests that substrate fluid migration pathways and traps are largely controlled by fault mechanics because quantifiable differences in chimney distribution are observed between compressional and extension deformation zones.

Geologic setting

The Hosgri Fault forms the southern half of the Hosgri/San Gregorio strike-slip fault system, which extends for approximately 400 km along the central California coast between Point Arguello and San Francisco (Figure 1; Sorlien et al., 1999; Lettis et al., 2004; Dickinson et al., 2005; Johnson and Watt, 2012). The Hosgri/San Gregorio is the westernmost active fault zone within the broader San Andreas Fault System, a broadly distributed, northwest–southeast-oriented transform plate boundary along the West Coast of the United States. The San Andreas Fault proper, located to the east of the Hosgri Fault, is the dominant fault within the transform boundary and has an estimated slip rate of approximately 30–36 mm/yr (McCaffrey, 2005; Meade and Hager, 2005; Titus et al., 2011). Faults to the west of the San Andreas Fault carry an estimated approximately 4–5 mm/yr of dextral slip (McCaffrey, 2005; Meade and Hager, 2005); Johnson et al. (2014) and PG&E (2014) use offset seabed morphology to constrain the late Pleistocene to present slip rate at approximately 2.6 and 1.75–1.90 mm/yr, respectively, for the section of the Hosgri Fault that passes through the study area.

Our investigation focuses on the HFZ offshore of Point Sal (Figure 1) using 3D seismic-reflection data collected by Pacific Gas and Electric (PG&E) in 2012 (Ebuna et al., 2013; PG&E, 2014). Previous work in the Point Sal area, based on single-channel high-resolution seismic-reflection and marine magnetic data, suggests that multiple fault strands characterize the HFZ, including an intersection with the northwest-trending Lions Head Fault (LHF; Figure 1; Johnson and Watt, 2012). Hansen et al. (2004) and Johnson and Watt (2012) map a Hosgri Fault "section boundary" near

the convergence of the Hosgri and LHF based on changes in fault trend and local deformation patterns.

The portion of the HFZ offshore of Point Sal underlies the Santa Maria River delta and is blanketed by a southward-thinning wedge of latest Pleistocene and Holocene sediment. A prominent erosional unconformity (inferred to be the transgressive surface) separates these young sediments from underlying older Quaternary deposits (Johnson and Watt, 2012; PG&E, 2014). A deeper angular unconformity separates the inferred Quaternary deposits from Neogene bedrock (Johnson and Watt, 2012; PG&E, 2014). Faulting and deformation commonly warp, cut, and offset Quaternary strata. Local basins and growth folds occur within and adjacent to the HFZ (Johnson and Watt, 2012). The 2012 high-resolution 3D seismic volume data from the offshore of Point Sal similarly reveal that this portion of the HFZ is characterized by fault bends, en echelon fault patterns, and structures that result from a relatively complicated deformation history (PG&E, 2014).

3D seismic reflection data acquisition and processing

In 2012, a 13.7 km^2 3D P-Cable seismic volume was collected as part of PG&E's Central California Seismic Imaging Project (PG&E, 2014). The high-resolution seismic reflection data were acquired using a triple-plate boomer source (1.75 kJ input power), with a seismic frequency range of approximately 100–700 Hz and a peak frequency of 200–225 Hz (PG&E, 2014). Seismic traces were recorded using an array of 14, eight-channel (6.25 group spacing) digital streamers connected to a single P-Cable towed perpendicular to the ship's heading (Nishenko et al., 2012; Ebuna et al., 2013). The 14 streamers were spread apart by towed paravanes providing a 14×8 (112 total) channel receiver array with a 43.75 m crossline width and a 50 m inline length. Sail lines were spaced 37.5 m apart and oriented northwest–southeast (338°/158°, Figure 1) and included a shot interval of 3.125 m, a sample interval of 0.25 ms (4 kHz sample rate), and a 0.75 s record length. This acquisition geometry produced eight-fold stacked sections with a 3.125×3.125 m bin size (PG&E, 2014). Seismic processing steps consisted of quality control checks, tidal corrections, velocity analysis, NMO correction, stacking, surface-related multiple elimination, deconvolution, crossline statics, and prestack time migration (Fugro Consultants Inc., 2012; PG&E, 2014).

The vertical resolution in the shallow substrate is approximately 2 m based on the dominant frequency and estimated 1600 m/s P-wave velocity (PG&E, 2014). It was determined that source characteristics and near-seafloor reverberation limited the vertical resolution at the seafloor to approximately 5 ms, or approximately 4 m (PG&E, 2014).

Data conditioning and seismic attribute workflow

Postprocessing data conditioning

Following PG&E's public release of data acquired by the Central Coastal California Seismic Imaging Project (e.g., PG&E, 2014), the 3D seismic volume located offshore Point Sal was downloaded in SEGY format from

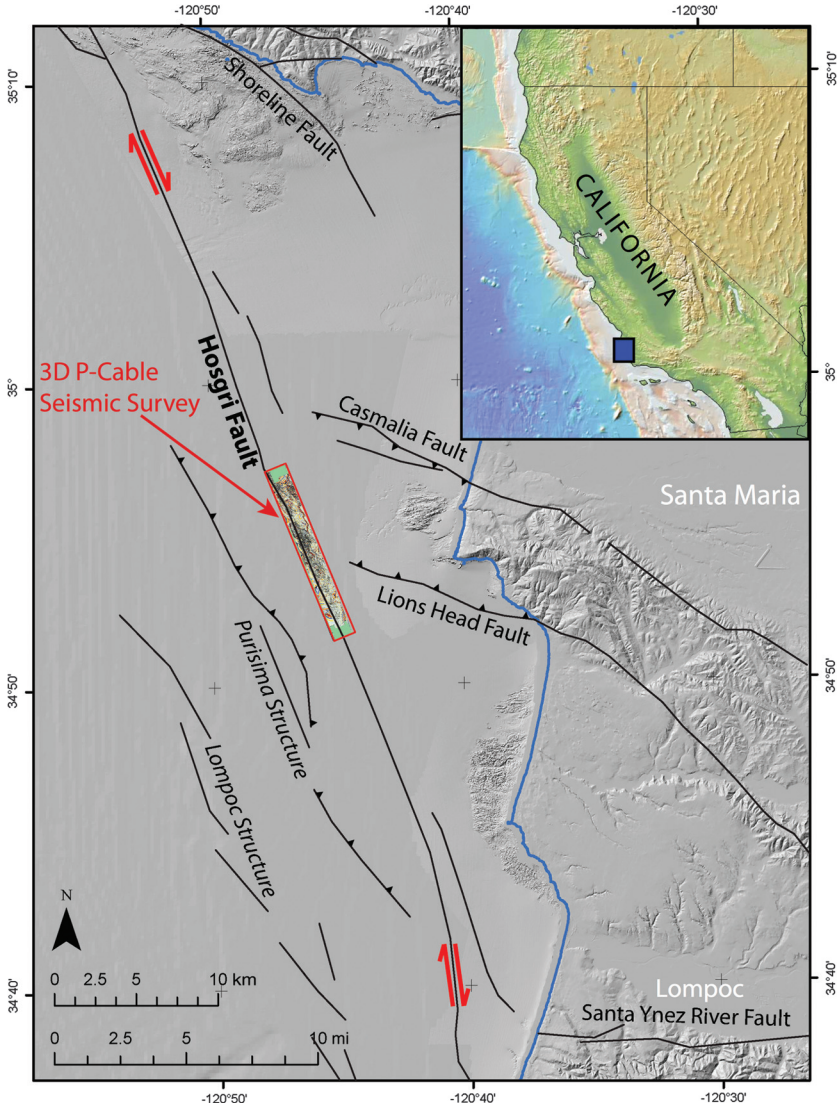

Figure 1. Regional map showing the location of the 3D seismic reflection data volume for offshore central California. The red rectangle denotes the location and extent of the 3D seismic volume along a portion of the Hosgri Fault. The black lines highlight the approximate locations of fault traces. The small blue box in the inset in the top right corner shows location of the regional map along the California coast.

the United States Geological Survey (USGS)'s National Archive of Marine Seismic Surveys. After preliminary analysis of data quality, a data conditioning workflow was developed to further enhance the quality and interpretability of the seismic volume. Initially, a dip-steering (structural steering) volume was calculated that contains the local dip and azimuth of seismic events at every sample position (Tingdahl et al., 2001; Tingdahl and de Rooij, 2005). The steering algorithm used a $1 \times 1 \times 1$ (inline, crossline, and sample interval) calculation step-out. In addition, a $1 \times 1 \times 1$ step-out median filter was applied to the steering calculation results. This procedure produced a smoothed 3D volume of structural information for all the seismic events.

Next, a dip-steered median filter (DSMF) was parameterized to reduce random noise. The filter utilized a 1×1 inline-crossline step-out and no time gate/window (0 ms). To evaluate noise suppression and potential signal removal, the filtered results (Figure 2c) were subtracted from the input (Figure 2a) to evaluate the signal removed during filtering (Figure 2b). As is shown in Figure 2b, a significant amount of noise oriented in the inline and crossline directions was isolated and removed, whereas the minimal desired signal was suppressed. The structurally filtered results provided a reduction of random and apparent acquisition noise, while preserving edges and enhancing laterally continuous events (Brouwer and Huck, 2011).

To enhance the detection and interpretability of faults, a dip-steered diffusion filter was applied to the DSMF data (Figure 2d). The dip-steered diffusion filter used a 1×1 (inline and crossline) step-out with no time gate (0 ms). The structurally steered diffusion filter replaced low-quality traces with surrounding traces of better quality and enhanced continuous edges, such as reflector offsets caused by faults. Figure 3c shows the sharpening of fault zones after the application of dip-steered median and diffusion filtering.

Last, a predictive deconvolution filter was parameterized and applied to the DSMF data in an attempt to suppress the apparent reverberation below the seafloor reflection (PG&E, 2014). Throughout the 3D seismic volume, the seafloor reflection suffers from a wide wavelength, and often masks near-surface phenomena (e.g., bright spots in Figure 4). The approach effectively suppressed the reverberation and also sharpened subbottom reflectors, yielding a slight increase in the resolvability of the seismic stratigraphy (Figure 4).

Seismic attribute workflows

We employed two separate attribute workflows to the preconditioned seismic data for the detection of faults and fluid-migration pathways (i.e., seismic chimney zones). The workflows used in this study utilized dip steering and neural networks. Dip steering improved the geometric attribute accuracy and object detection power by providing structural information (e.g., dip and azimuth) during attribute calculations. The structural information was particularly useful in this study because of the dense network of faults and steeply dipping strata associated with deformation.

The supervised neural-network module used in this study is a fully connected multilayer perceptron with one hidden layer. The algorithm used back propagation with momentum and weight decay. Attribute weights were multiplied by a weight decay factor to produce smoother functions with improved generalization properties (Aminzadeh and de Groot, 2004; Brouwer et al., 2011). Supervised training consisted of user-defined picks along a desired target (e.g., faults and chimneys) and picks along nontarget examples within the 3D seismic volume. The neural network was then trained, and the data were split into training and testing vector sets (Figure 5). The error of the training vectors was used to update the weights, and the test vectors were used to check performance and avoid overfitting. Training was stopped when the error on the test vectors was minimal, the point at which the neural network has optimal generalization capabilities (Aminzadeh and de Groot, 2004; Brouwer et al., 2011). The generated meta-attribute results represent a measurement of relative probability for the desired target (e.g., chimney, fault, mass slide deposit, and salt body) that ranges between zero and one, with one representing the highest probability.

Neural-network fault cube

The 32 attributes, including multiple instances of some attributes with different parameters, were used as input nodes into the calculation of the neural-network fault cube meta-attribute. The hidden layer of the supervised neural-network consisted of 16 nodes. Table 1 lists the various attributes and weights used during neural-network training. Various parameterizations of the similarity attribute were used as weighted input nodes, as well as attributes, such as curvature, noise, average frequency, and others (Table 1). Multiple attributes utilized structural information and various step-out ranges. Approximately 2000 picks of fault and 3300 picks of nonfault examples were used for supervision of the neural-network training (Figure 5). Training was stopped when the normalized root-mean-square (rms) error of the train and test sets reached a minimum value (i.e., before the rms error trend shifted upwards, indicating overfitting), as well as the misclassification percentage. Input vectors were balanced using 1% noise. Post training, a seismic volume was generated that contained fault meta-attribute probability measurements output from the meta-attribute calculation. Fault and nonfault probabilities were then projected along inlines, crosslines, and z-slices within the 3D seismic volume. This allowed for the examination and correlation of probable faults to reflector offsets observed on amplitude data, helping to evaluate the validity of the neural-network fault attribute results (Figure 2h).

Neural-network chimney cube

The 36 attributes were used as input nodes into the supervised neural-network chimney calculation, and each node was weighted during the neural-network training. Similar to the fault meta-attribute calculation, the hidden layer with the chimney meta-attribute calculation consisted of 18 nodes, or half of the input nodes. Table 2 lists the different attributes and assigned

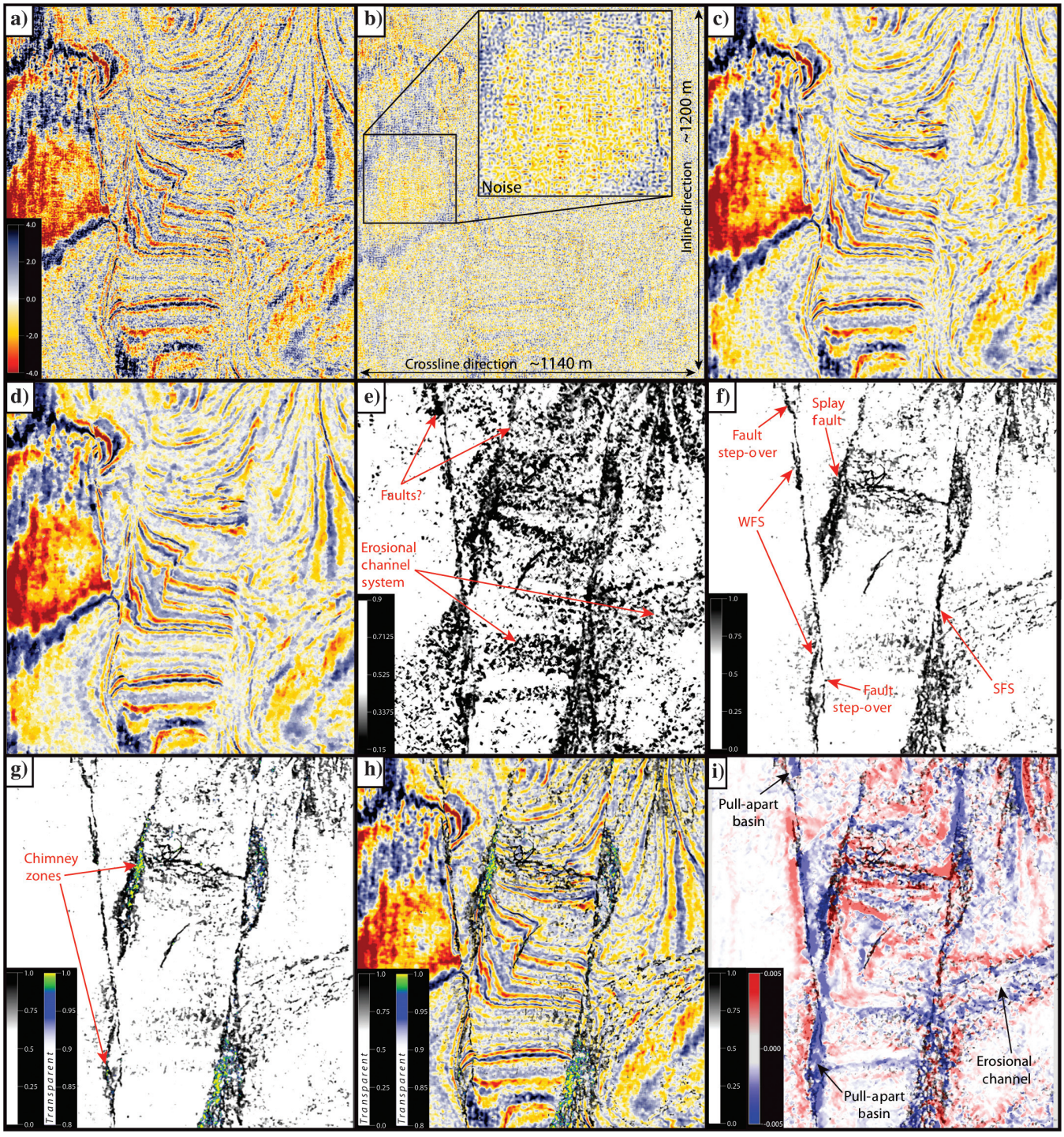

Figure 2. Multiple panels showing examples of the data conditioning and neural-network attribute steps along a subsection of a z-slice at 174 ms. (a) Input data, (b) noise extracted, and the inset shows expanded view of noise oriented in inline and crossline directions, (c) results after noise suppression using a DSMF, (d) dip-steered diffusion filtering applied to DSMF results, (e) dip-steered similarity attribute results, (f) neural-network fault attribute results, (g) neural-network chimney attribute results corendered with the fault-attribute results, (h) combination of fault and chimney attribute results corendered with DSMF amplitude data. (i) DSMF maximum curvature attribute with 50% transparency superimposed over the neural-network fault attribute results. Figure location is indicated by TH dashed red lines in Figure 6. SFS, southern fault strand and WSF, western fault strand.

weights used during the training procedure. The chimney meta-attribute input nodes used attributes tailored to criteria that characterize seismic chimneys, such as verticality (vertically parameterized attributes), discontinuity, chaos, frequency anomalies, and others (Brouwer et al., 2011). Approximately 1800 picks of chimney and 2400 picks of nonchimney were used to help to train the neural-network calculation. Similar to the neural-network fault attribute approach, training was stopped when the rms error reached minimum values along with a misclassification percentage of user picks. Input vectors were balanced using 1% noise. A few of the highest weighted attributes observed in the neural-network chimney calculation were parameterized similarity attribute calculations, the "simple chimney attribute," average frequency, median filter polar-dip, and variance (Table 2). The simple chimney attribute utilized a combination of similarity calculations tailored for verticality measurements.

Maximum curvature

In addition to the neural-network attribute workflows, maximum curvature (K_{max}) was calculated assuming a velocity of 1600 m/s. An inline-crossline step-out of 10 was used during the calculation, and a DSMF was applied to the results. The maximum curvature calculation can be used in conjunction with the fault cube to delimit fault and fold geometries and to extract information on sense of vertical throw across faults (e.g., Figure 2i; Roberts, 2001).

Interpretation

Fault meta-attribute and maximum curvature

Results from the neural-network fault attribute calculation show improvement in fault detection over single discontinuity attribute calculations within the high-resolution 3D seismic volume. The fault-probability attribute results provide better isolation of the desired fault detection while also maintaining or creating greater contrast along imaged fault strands. Figure 2 underscores such improvement in fault detection and isolation along a subsample of the 174 ms z-slice also shown in Figures 6 and 7. Using the single dip-steered attribute approach, multiple unwanted seismic discontinuities are enhanced, including lateral discontinuities caused by erosional incision and folded, steeply dipping strata (Figure 2e). By applying the trained neural-network meta-attribute calculation, portions of the unwanted discontinuities are suppressed, which improves the resolvability of desired fault strands and smaller scale fault complexities, including features such as subtle fault bends, junctions, and step-over segments (Figure 2f). In addition, fault strands with weak contrast using the single attribute calculation show a higher con-

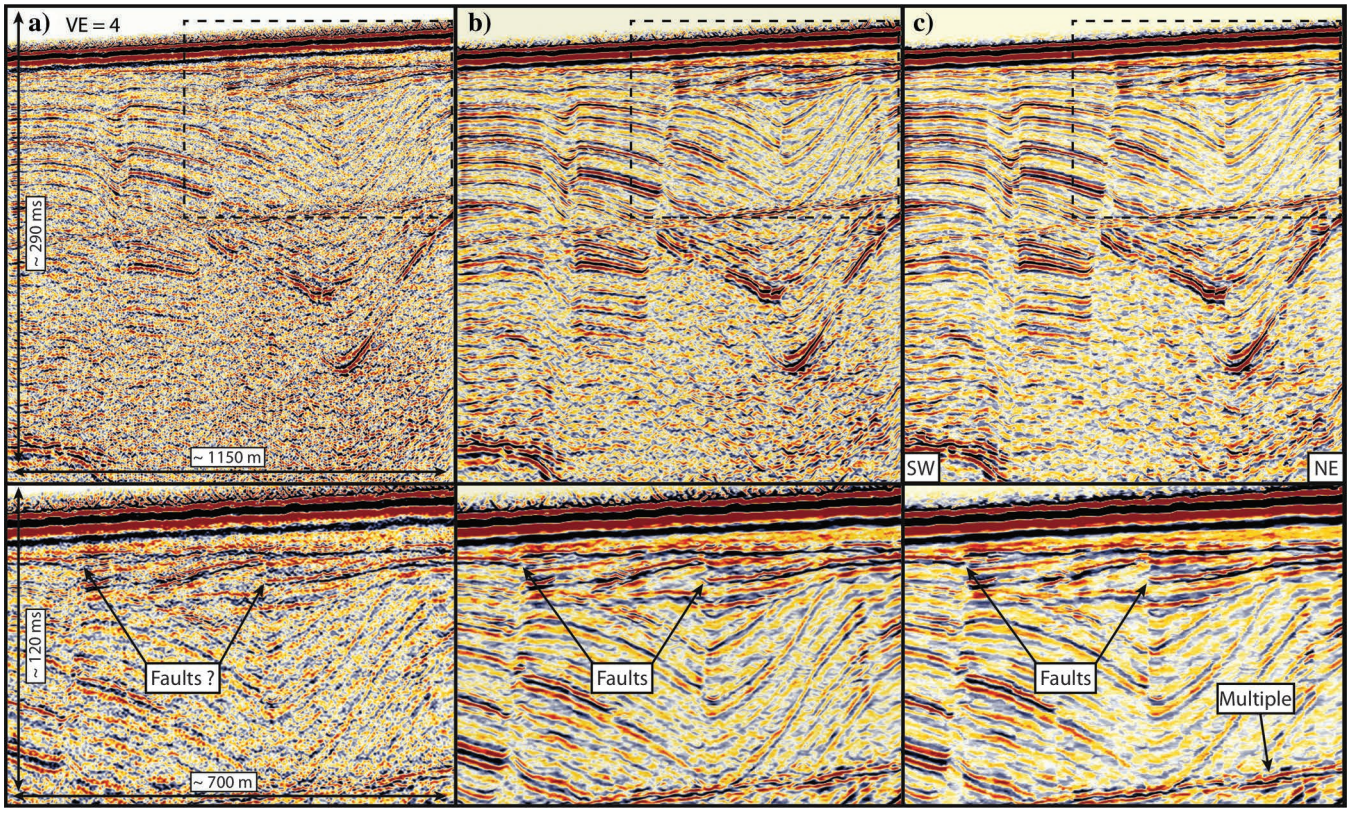

Figure 3. Example of a 2D crossline illustrating the improvement of fault detection using structural filtering. (a) Input data, (b) DSMF data, (c) DSMF data with dip-steered diffusion filtering. Insets below show enlarged portions of the profiles outlined by the dashed black boxes above. Note the improved imaging and sharpening of faults. The 2D profile location is outlined by the dashed horizontal red line (crossline) in Figure 6. VE, vertical exaggeration.

trast and are more continuous in the neural-network fault attribute result (Figure 2). A color scheme that grades into transparency for probabilities less than approximately 60% allows for improved visualization, evaluation, and interpretation of the fault attribute results superimposed on filtered amplitude data (Figure 2h). Maximum curvature corendered with the fault attribute provides additional structural information, such as fault throw. Figure 2i highlights such patterns, displaying the upthrown and downthrown sides of detected fault traces along a horizontal z-slice at 174 ms.

Projection of the fault probability attribute calculation across horizontal z-slices reveals a complex network of faults that span the length of the 3D seismic volume (Figure 6c). A z-slice at 174 ms two-way traveltime reveals single fault strands at the northern and southern edges of the 3D volume. These faults are referred to as the northern and southern fault strands (NFS and SFS), and they appear to be the master strike-slip faults of the HFZ within the survey region. There is an approximately 6° difference in strike between the NFS and SFS (330° and 336°, respectively; PG&E, 2014) and a complicated network of splayed and convergent fault strands throughout the intervening area (Figure 6c). The westernmost fault strand (WFS) splays off of the SFS and can be traced for more than 5 km to the north within the central portion of the seismic survey. The trace of the WFS is characterized by a series of right steps that appear to be associated with small pull-apart structures as highlighted by the maximum curvature attribute as downthrown fault zones (Figure 2i). In addition, shorter, secondary faults splay off of the WFS to the north. The HFZ widens (approximately 1 km) and becomes highly distributed to the north, where fault identification becomes complicated by broad patches of high discontinuity (Figure 6c) and complex curvature results (Figure 7b). Just north of the broadest point, secondary fault strands quickly converge to the west, where the fault attribute results become chaotic and dispersive. A large discontinuity zone with strong curvature amplitudes converging from the southeast also complicates this region, intersecting the chaotic fault zone within the central portion of the 3D volume (Figure 7b).

The large discontinuity zone converging from the southeast is identified as the LHF (Figure 6c). The intersection of the LHF coincides with the northern termination of the WFS and associated splayed faults in the southern half of the 3D volume. High curvature amplitudes are observed in this region (Figure 7b). To the west of the LHF and HFZ intersection point, a continuous and sharply defined fault emerges from the western edge of the 3D volume and converges with the NFS. This fault strand is interpreted to be a PFB due to fault convergence, and it will be described in greater detail in the following sections. North of the confluence between the PFB and the NFS, another fault zone emerges from the southeast and intersects the HFZ near the northern edge of the 3D volume (Figures 6c and 7b). This fault zone was also identified by PG&E (2014) and was inferred to be the near-surface expression of a blind thrust fault (BTF). The NFS of the HFZ extends to the northwest corner of the 3D volume; however, lack of coverage to the east prevents additional analysis of the BTF intersection (Figure 6).

Chimney meta-attribute

The neural-network chimney attribute results provide additional insight into potential fluid/gas migration zones present within the 3D seismic volume. As with the fault attribute results, the chimney results can be projected along a z-slice for plan-view analysis of the distribution of probable fluid-migration pathways. Figure 2g shows an enlarged section of the neural-network chimney attribute calculated along a portion of the 174 ms z-slice. A gradational color scale with transparency reveals only the highest (approximately 90% and above) chimney probabilities, allowing for visual inspection of several attribute calculations along the same surface (Figures 2h and 7a). By projecting the chimney results along vertical inlines and crosslines, it becomes evident that zones of high chimney proba-

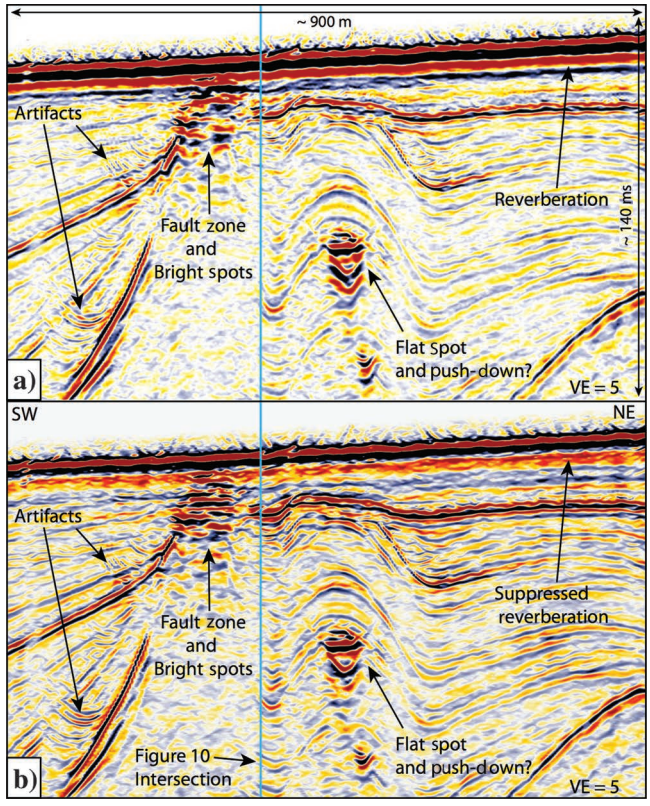

Figure 4. Subsection of a 2D crossline showing indicators of gas/fluid and results from poststack predictive deconvolution. (a) DSMF data, (b) DSMF data with poststack predictive deconvolution. Note the apparent flat spot and possible velocity push-down. The location is outlined by the solid black line in Figure 6. The intersection of Figure 10 is delineated by the solid blue line. VE, vertical exaggeration.

bility commonly terminate at the base of shallow bright spots (e.g., Figure 8).

Visualization of the chimney attribute results in conjunction with the fault attribute results reveals a strong correlation between faults and potential fluid-migration pathways throughout the study region. For example, the chimney attribute results projected along a z-slice at 174 ms shows a strong connection between detected faults and chimney distribution (Figure 6d). Within the southern half of the 3D volume, high-probability chimney zones are predominantly concentrated along discrete faults. Figure 2g and 2h is the example of high-probability chimney zones present along portions of detected fault strands, and Figure 9b is a 3D perspective view of the same region. To the north, where the WFS-splayed fault zone widens to approximately 1 km, the chimney signals become more disperse, with some regions exhibiting large chimney clusters that span across separate splayed fault strands (Figure 6d).

The confluence of the LHF and the HFZ/NFS is associated with broad patches of high chimney probability that nearly extend to the western edge of the 3D volume (Figures 6d and 9d). Although the dense chimney zone diminishes as the NFS and the PFB become sharply defined and discrete fault strands, high chimney probabilities and clusters of shallow bright spots are observed in and around the confluence of the two faults (Figures 6d and 8). Folding and an apparent flat-spot at the apex of an anticline are also observed in this region (Figure 4), and this is suggestive of significant fluid-focusing and trapping. Furthermore, zones with anticlinal folding, such as the LHF and PFB zones, commonly show strong maximum curvature amplitudes (Figure 7b). Additional zones of high chimney probability are observed along the NFS and along the projected BTF as it emerges from the southeast (Figure 6d).

Relationship among faults, deformation, and probable fluid pathways within an active strike-slip shear zone

Attribute results indicate a strong connection between the dominant mode of deformation and the probability for gas chimneys and/or fluid pathways. In the following interpretive sections, we break the 3D study area into three zones: (1) a transtensional zone that characterizes the southern end of the survey region, (2) a transpressional zone located near the center of the 3D volume, and (3) the LHF/BTF intersection zone within the northern half of the study area (Figures 7c and 9). For additional structural details, mapped horizons, and estimated slip rates, see PG&E (2014). In addition, Figure 6–28 in PG&E (2014) provides a comparison with previous lower resolution mapping within the region.

1) Examination of offset reflectors in the southern region of the 3D seismic volume and maximum curvature results suggests that the faults have oblique kinematics, with observed dip-slip in the normal direction (Figures 3, 7b, and 10). Continuous, parallel, and subparallel reflectors within a sedimentary basin located near the southern end of the survey (Figure 10) are cut by faults branching off of the WFS (Figures 2h and 6b); reflectors are displaced in the horizontal and normal directions, creating small, localized depressions along the fault strands. These downthrown regions are highlighted on z-slices by corendering the fault attribute with maximum curvature (Figures 2i and 7b). Based on these observations, and comparison with interpretations by PG&E (2014), this section of the HFZ appears to be dominated by transtensional deformation (Figure 7c). Chimney attribute results generally show the highest probability along discrete faults in places dominated by transtension, suggesting that upward fluid migration is mostly confined to fault-generated permeability path-

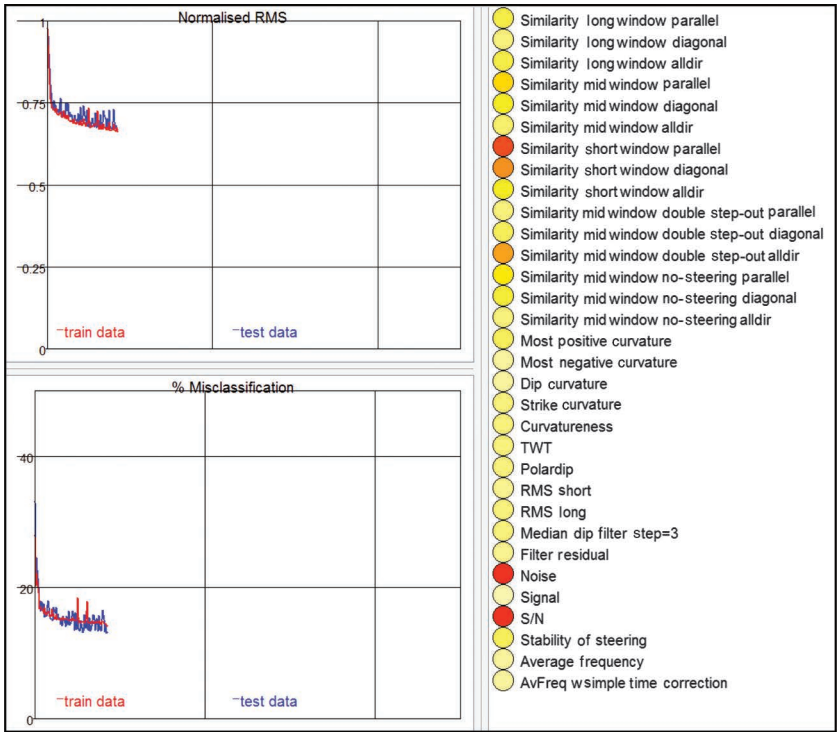

Figure 5. Example of neural-network attribute training window. The top-left panel shows normalized rms values during training. The bottom-left panel shows the misclassification percentage of user picks during training. The right panel shows attribute node weights during training, with warmer colors representing higher weights. This example was paused during training, and the attribute weights do not correlate to those in Tables 1 and 2.

ways (Figures 2g and 9b). High chimney probabilities are observed along the northern extension of the SFS (Figures 6d and 9b), but they diminish along the fault toward the north, where the deformation zone between the SFS and the WFS widens to more than 1 km. As chimney probabilities decline northward along the SFS, more disperse zones of strong chimney signal appear in the substrate between individual faults (Figure 6d). This broad zone of higher chimney probabilities also coincides with the onset of compressional folding (Figures 7c and 10).

Table 1. List of attributes used in the neural-network fault attribute calculation. Individual attributes or parameterizations of attributes are listed in the left column. The right column lists attribute weights used during the neural-network training.

Attribute nodes	Weight percentage
Similarity long-window parallel	14.9
Similarity long-window diagonal	20
Similarity long-window all directions	23.3
Similarity midwindow parallel	35.6
Similarity midwindow diagonal	22.8
Similarity midwindow all directions	38.6
Similarity short-window parallel	37.6
Similarity short-window diagonal	32.7
Similarity short-window all directions	37.4
Similarity midwindow double step-out parallel	13.3
Similarity midwindow double step-out diagonal	23.6
Similarity midwindow double step-out all directions	33.1
Similarity midwindow no-steering parallel	28.4
Similarity midwindow no-steering diagonal	22.6
Similarity midwindow no-steering all directions	29.1
Most-positive curvature	12.8
Most-negative curvature	10.7
Dip curvature	8.6
Strike curvature	6.1
Curvatureness	21.8
TWT	10.8
Polar dip	16.3
rms short	40.5
rms long	10.4
Median dip filter step = 3	10.6
Filter residual	9.4
Noise	100
Signal	13.6
S/N	72.7
Stability of steering	19.6
Average frequency	6.5
Average frequency with simple time correction	9.3

2) Across the central part of the 3D survey inline and crossline, seismic profiles show evidence of folding and uplift within the HFZ (e.g., Figures 9c and 10). The uplifted strata form anticlinal folds that are cut by various fault strands of the HFZ. Within this zone,

Table 2. List of attributes used in the neural-network chimney attribute calculation. Attribute names are provided in the left column, and attribute weight percentages used during training are listed in the right column.

Attribute nodes	Weight percentage
Similarity parallel [−40, 40]	32.1
Similarity diagonal [−40, 40]	29.4
Down 100 ms similarity parallel [−40, 40]	16.9
Up 100 ms similarity parallel [−40, 40]	27.6
Down 100 ms similarity diagonal [−40, 40]	17.6
Up 100 ms similarity diagonal [−40, 40]	17.1
Similarity all directions [−40, 40]	54
Down 100 ms similarity all directions [−40, 40]	16.8
Up 100 ms similarity all directions [−40, 40]	21.8
Simple chimney attribute	44.3
No neural-network input polardip	18.1
rms [−40, 40]	30.4
Down 100 ms rms [−40, 40]	35.9
Up 100 ms rms [−40, 40]	8.7
No neural-network input filter residual	18.4
No neural-network median dip filter step-out = 3	6.9
Noise rms [−40, 40] filter residual	39
Down 100 ms noise	28.2
Up 100 ms noise	33.2
No neural-network input rms [40, 40] median dip filter	26.5
Signal/noise	36.7
Down 100 ms signal/noise	18.2
Up 100 ms signal/noise	27.1
TWT	37.3
Average frequency	40
Average frequency with simple time correction	34.1
Median filter polar dip	100
No neural-network low-pass	10.6
No neural-network rms low-pass	18.7
No neural-network high-pass	9.3
No neural-network rms high-pass	28.9
Frequency washout ratio	17.6
Variance [−40, 40] polar dip	56.8
Frequency washout ratio with simple time correction	15.9
Down 100 ms variance [−40, 40] polar dip	30.5
Up 100 ms variance [−40, 40] polar dip	18.5

the major unconformity that separates older Neogene rocks from younger Quaternary sediments is clearly folded and uplifted (e.g., Figure 6–33 in PG&E, 2014), and in some regions, this unconformity nearly reaches the seafloor (Figure 10). Relative to the southern extent of the 3D volume, chimney

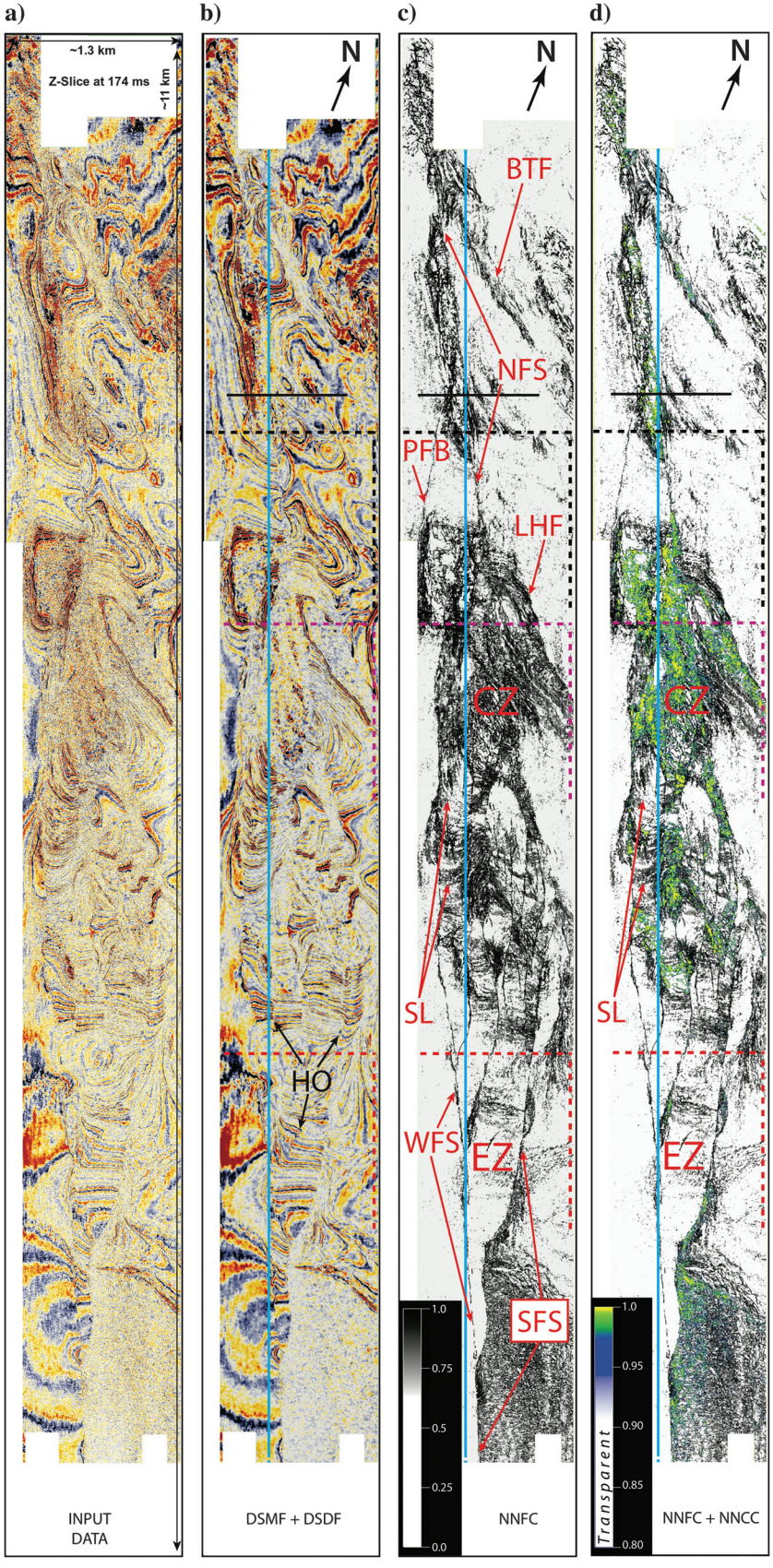

Figure 6. Multiple z-slice panels at 174 ms showing data enhancement and attribute results. Panels have been rotated 22° clockwise from true north. (a) Input data, (b) DSMF and diffusion filtered data, (c) neural-network fault attribute results, (d) neural-network chimney attribute results corendered with fault-attribute results. The dashed red lines show the location of Figures 2, 9a, and 9b. The dashed purple lines show the location of Figure 8c and 8d. The dashed black lines show location of Figure 8. The solid blue line denotes the location of Figure 10, and the solid black line displays the location of Figure 4. NFS, northern fault strand; SFS, southern fault strand; WFS, western fault strand; EZ, extensional zone; SL, structural leakage; CZ, compression zone; LHF, Lions Head Fault; PFB, paired fault bend; BTF, blind thrust fault; HO, horizontal offsets; DSMF, dip-steered median filter; DSDF, dip-steered diffusion filter; NNFC, neural-network fault cube; and NNCC, neural-network chimney cube.

attribute results show a widespread distribution of high probabilities in the areas between faults (Figure 6d), particularly within fault-bounded structures typically associated with transpression, such as growth folds, anticlines, and steeply dipping reverse faults (e.g., Figure 9d). Maximum curvature amplitudes are also very high in this region, and these results help to characterize the folded regions on z-slices (Figure 7b). Based on these observations, the central region appears to be dominated by transpressional faulting and folding (Figure 7c), an interpretation also proposed by PG&E (2014) (e.g., Figure 6–33 in PG&E, 2014).

3) The northern part of the 3D volume is complicated by the convergence of the LHF and BTF with the NFS. Where these faults converge with the NFS, transpressional deformation is observed (Figures 7c, 9c, and 10), and the convergence appears to have generated a type of "PFB," similar to the models proposed by Mann (2007) and Johnson and Watt (2012). For example, farther north along the HFZ, Johnson and Watt (2012) propose that a PFB formed west of the HFZ due to indentation of a rigid basement block between the HFZ and the shoreline fault (Figure 1). Similarly, we propose that the convergence of the LHF and the HFZ (or more specifically, the NFS) forms an impinging "block zone" and developed a PFB to the west of the convergence zone. The leading restraining and trailing releasing bends associated with this zone of impingement have subsequently led to compression and extension (Figure 10) within the region bounded by the PFB and the NFS (Figure 7c). High chimney probabilities and numerous shallow bright spots are associated with the compressional portion of the PFB (Figures 7c, 6d, and 9d). To the north, where the interpreted BTF (PG&E, 2014) converges with the NSF, another zone of compression and uplift is observed (Figures 7c and 10). Chimney attribute results indicate a more fault-focused distribution in this region except on the northernmost portion of the 3D volume, where the fault, chimney, and curvature attributes exhibit a dispersive pattern. Although limited by data coverage, numerous shallow bright spots are observed above these high-probability chimney zones.

Along the portion of the HFZ imaged in this study, substrate fluid concentration appears to be closely tied to the kinematics of strike-slip faults and the associated structural deformation. Transtension along the HFZ in the southern portion of the 3D survey area promotes normal-oblique motion along the fault strands, resulting in subsidence and sedimentary infill (Figures 9a and 10). Subsidence displaces fluid-rich rocks located below the Neogene-Quaternary unconformity (i.e., the Monterey Formation; Pisciotto and Garrison, 1981; Isaacs et al., 1983) farther away from the seafloor. Compaction of the relatively thick section of concordant

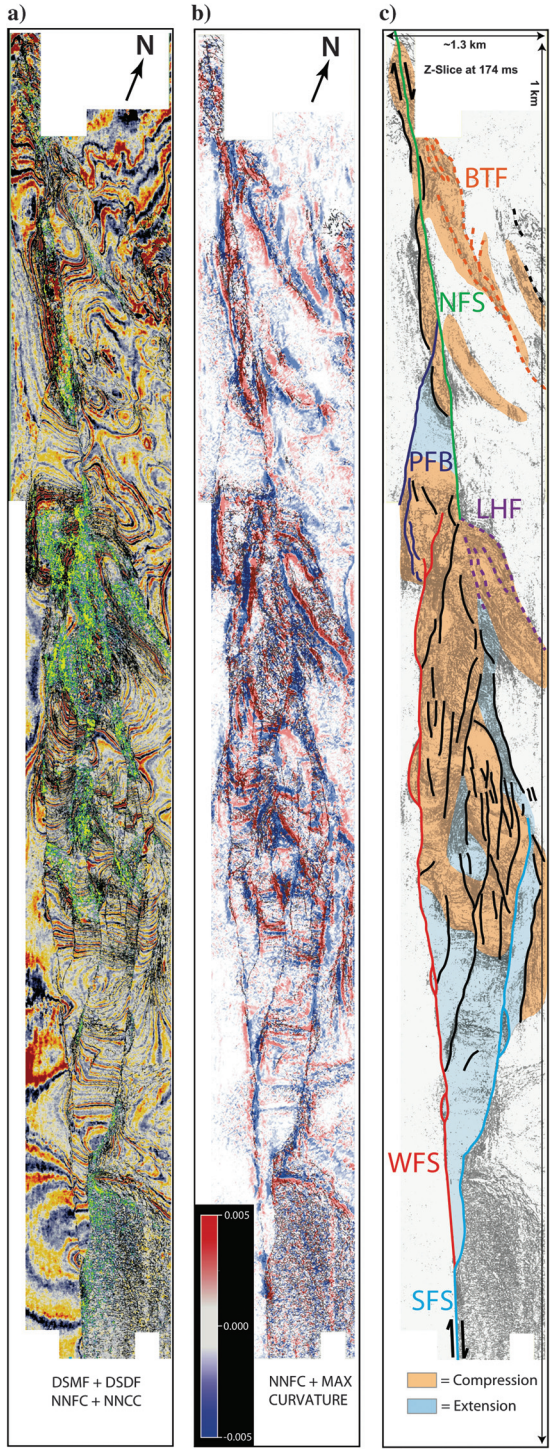

Figure 7. Some z-slices at 174 ms showing corendered neural-network attribute results, maximum curvature, and structural interpretations. (a) Neural-network fault and chimney attribute results with a transparency color scheme on top of structurally filtered seismic amplitude data, (b) DSMF maximum curvature attribute with 50% transparency superimposed over the neural-network fault attribute results. (c) Structural interpretation of faults and regions of compression and extension. NFS, northern fault strand (green); SFS, southern fault strand (blue); WFS, western fault strand (red); LHF, Lions Head Fault (dashed purple); PFB, paired fault bend (dark blue); and BTF, blind thrust fault (dashed orange). The black lines represent smaller unnamed faults within the survey region.

parallel and subparallel bedded sedimentary infill may force fluids to migrate horizontally toward the fault-bounded margins of the transtensional zones. Because extensional faults have lower confining normal stress (e.g., Means, 2012), it is conceivable that they act as least resistance fluid-flow pathways and provide a focused migration route to the seafloor. In contrast, transpression in the central and northern regions of the 3D study area is linked to folds, anticlines, and uplifted sections of older fluid-rich rocks, bringing the Neogene-Quaternary unconformity to just below the seafloor in a few locations. The transpressional folds appear to create fluid traps and localized reservoirs except where they are cut by multiple strands of the HFZ (e.g., Figure 9d). The combination of transpressional folding and strike-slip faulting appears to promote structural trapping and fluid-escape pathways along faults that cut through the traps. Statistical analysis of chimney attribute results along subsections of the transtensional and transpressional zones reveals a substantially higher probability for chimneys in areas dominated by transpression (Figure 11).

Transpressional deformation is most apparent along strike-slip restraining bends and fault-convergence zones, such as the NFS-LHF and subsequent PFB. Other studies of offshore California have also documented seafloor seepage along strike-slip fault restraining bends and step-overs (e.g., Hein et al., 2006; Paull et al., 2008; Maloney et al., 2015). Similarly, fault-controlled seepage patterns have been recently observed within the Marmara Sea along the North Anatolian Fault System. Seeps appear to be concentrated along discreet faults in transtensional zones, but are widely distributed in transpressional zones (i.e., anticlinal features; Dupré et al., 2015). However, through the use of advanced attribute analyses, this study provides high-resolution insight into 3D patterns of structural deformation (i.e., formation of traps and fluid reservoirs) and associated fluid migration pathways along a transpressional section of an active strike-slip fault.

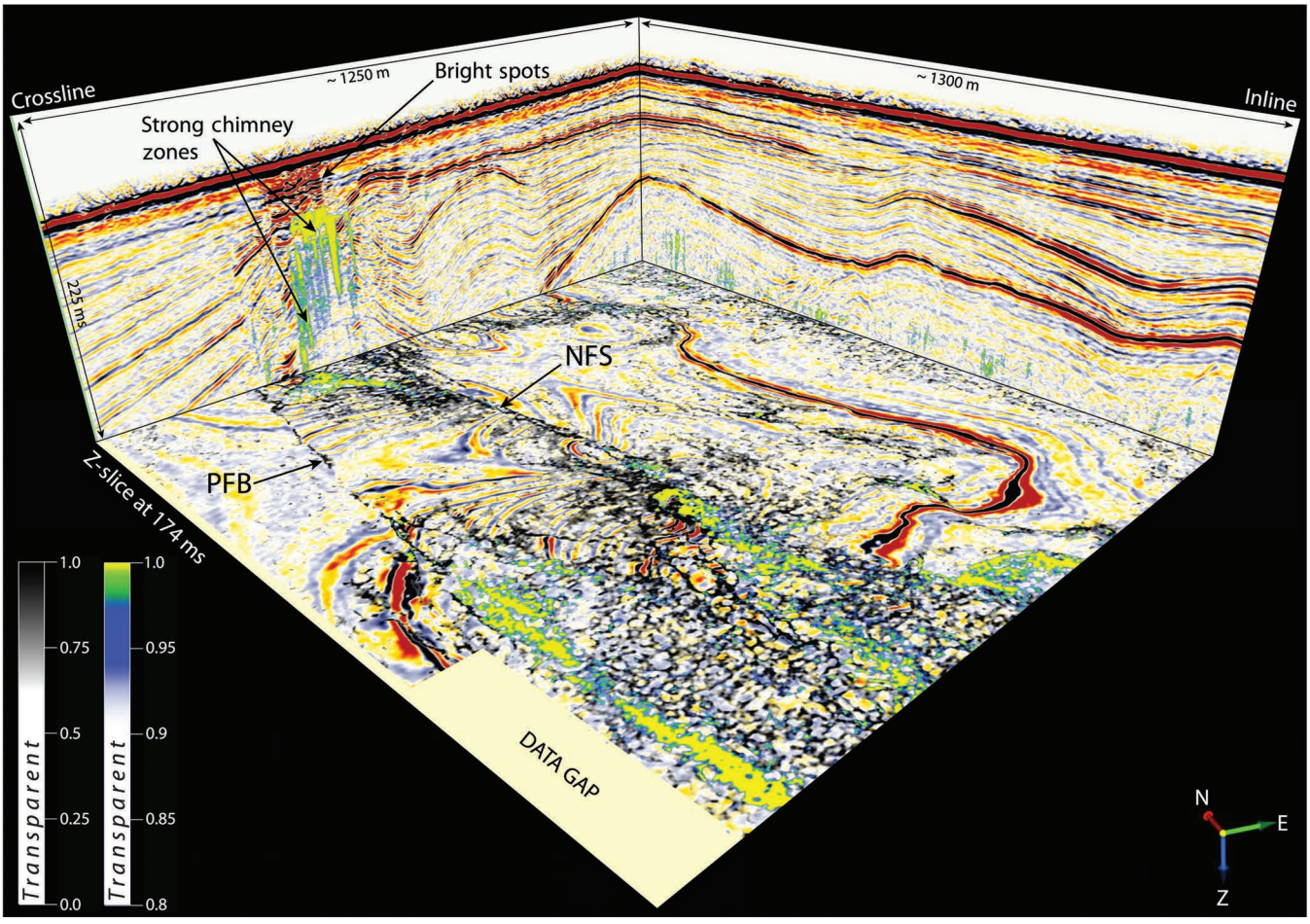

Figure 8. A 3D perspective view of the PFB region showing the neural-network fault and chimney attribute results. Fault and chimney attribute results along a z-slice at 174 ms show relationship between faulting and chimneys. Chimney attribute results are also projected onto vertical inlines and crosslines. Note the termination of a dense zone of high-chimney probabilities below shallow, abruptly ending high-amplitude reflectors interpreted as bright spots. Location provided by dashed black lines in Figure 6. NSF, northern fault strand and PFB, paired fault bend.

Potential pitfalls and future work

Although the neural-network seismic attribute workflows provided new insights into the distribution of probable faults and fluid-migration pathways, some potential pitfalls or limitations must be discussed. Similar to the "structural leakage" artifact discussed by Marfurt and Alves (2014), regions with steeply dipping strata or a poor seismic signal can complicate discontinuity attribute calculations, and such zones are present within the transpressional segments of the HFZ in this study (e.g., Figures 6c and 10). Such features can exaggerate the probability values in the fault-attribute results. Although the neural-network results reduce unwanted discontinuities (especially when compared with single-attribute approaches; Figure 2e and 2f), reflections associated with high-angle dipping strata can be of lower quality and lower amplitude, and they may fail to register in the structural (steering) calculation. The result is unwanted discontinuity returns during structurally steered fault-attribute calculations. Fortunately, steeply dipping strata are commonly associated with circular-to-elliptical fold structures and typically show a contourlike pattern on horizontal z-slices, allowing them to be easily identified and interpreted as unwanted artifacts (e.g., "SL" in Figure 6c).

Because the neural-network chimney attribute calculation is heavily dependent on measurements tailored to verticality, regions of low seismic quality from

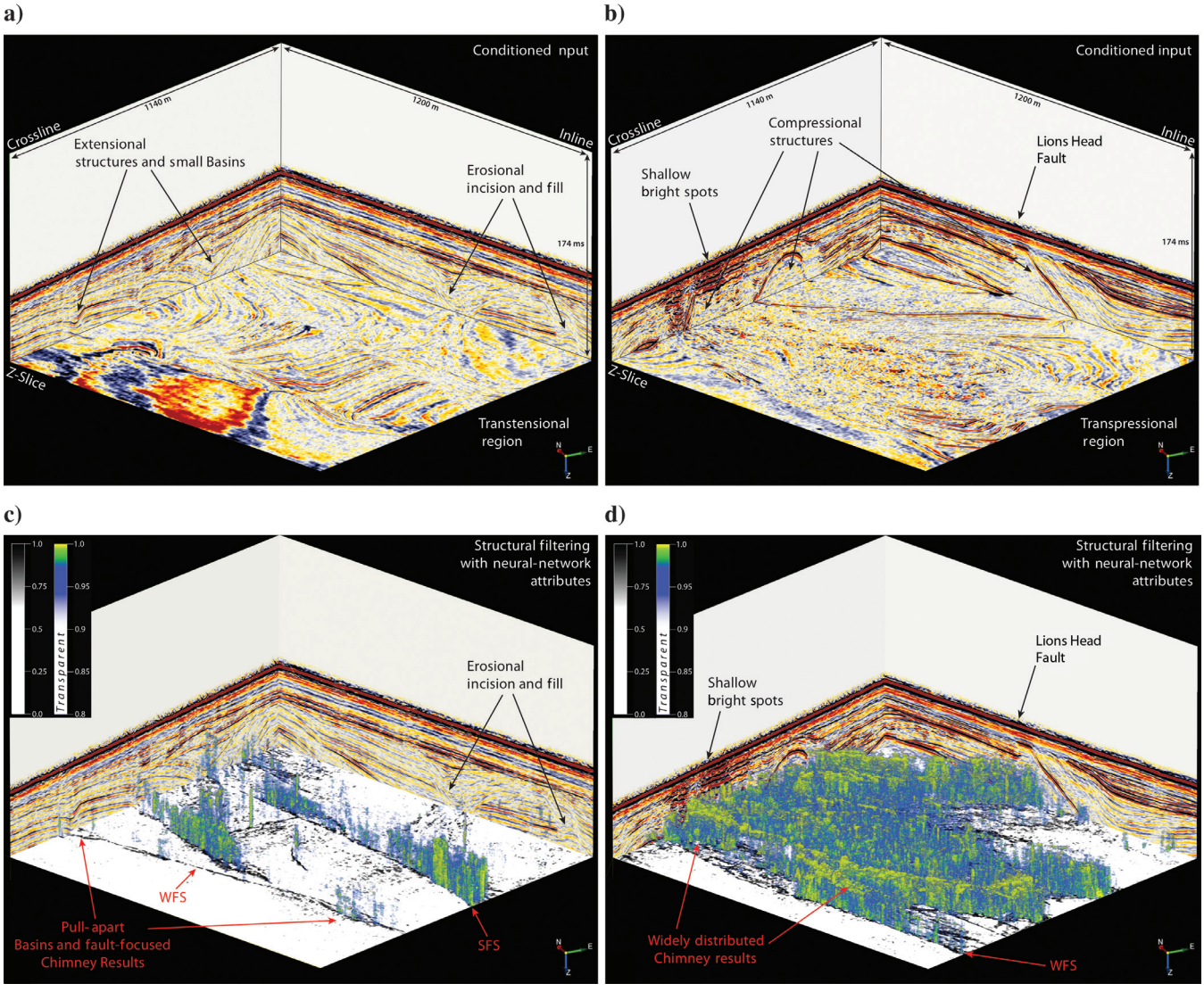

Figure 9. Three-dimensional perspective views showing 3D volume rendering of neural-network chimney attribute results along the transtensional and transpressional zones within the 3D seismic volume. (a) View of inline, crossline, and z-slice (174 ms) within the transtensional region, (b) transtensional region with fault attribute projected along the z-slice and a 3D volume rendering of the chimney attribute results, (c) view of filtered data within a transpressional region. (d) Transpressional region with fault-attribute results along the z-slice and 3D rendering of the chimney attribute above. Note the differences in abundance and distribution of high chimney probabilities between the two different regions. WFS, western fault strand and SFS, southern fault strand. The locations are outlined by the dashed red (panels a and b) and purple (panels c and d) lines in Figure 6.

steeply dipping strata can also produce unwanted high chimney probabilities. Again, structural leakage zones may complicate the targeted attribute analysis and lead to unrealistic interpretations. Although the chimney attribute results calculated in this study along the HFZ likely contain regions of unwanted high probabilities, these zones of apparent structural leakage can also be identified by the interpreter and discarded. Seismic chimneys and bright spots are commonly considered seismic indicators of fluid flow and leakage anomalies (e.g., Løseth et al., 2009). Our results indicate that regions of high chimney probability commonly terminate upwards into the base of shallow bright spots (Figures 8 and 9d). This correlation helps to strengthen the viability of the neural-network chimney attribute results presented herein. However, the validity of the chimney attribute results would be improved with additional criteria, such as geochemical data and

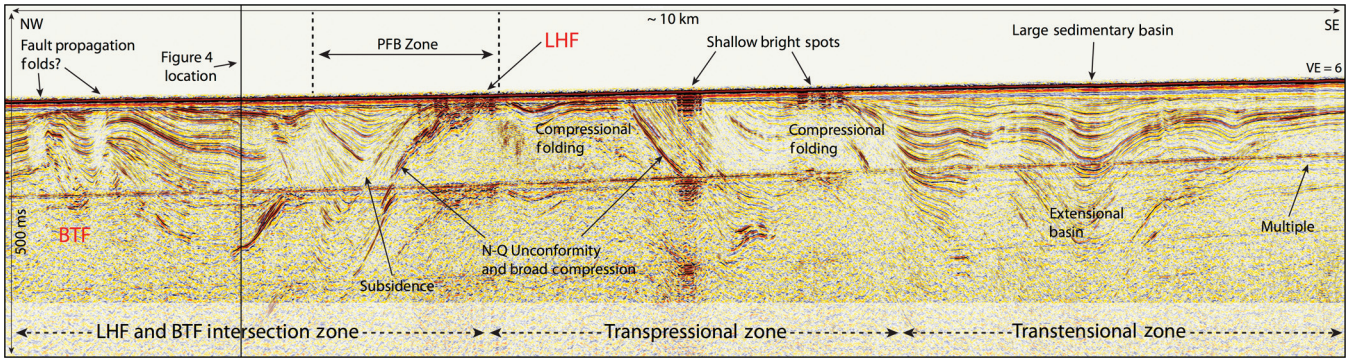

Figure 10. Two-dimensional inline through the HFZ. Inline shows three defined structural regions: the transtensional zone in the southern portion of the survey, transpressional zone near the central region, and the LHF/BTF intersection zone in the northern half of the survey. Note regions of apparent subsidence (transtensional) and uplift (transpressional). The location of the inline is delineated by the solid blue line in Figure 6. N-Q, Neogene-Quaternary; LHF, Lions Head Fault; BTF, blind thrust fault; PFB, paired fault bend; and VE, vertical exaggeration.

Figure 11. Histogram plots of the neural-network chimney attribute results from the *z*-slices shown in Figure 9. Top histogram shows the chimney probability values from the transtensional region (Figure 9b), whereas the bottom histogram plot shows the probability values from the transpressional zone (Figure 9d). Note the abundant signal near zero in the transtensional zone, indicating numerous chimney values with low probabilities. In contrast, the histogram plot from the transpressional region shows an abundant signal near one, indicating numerous chimney signals with high probabilities.

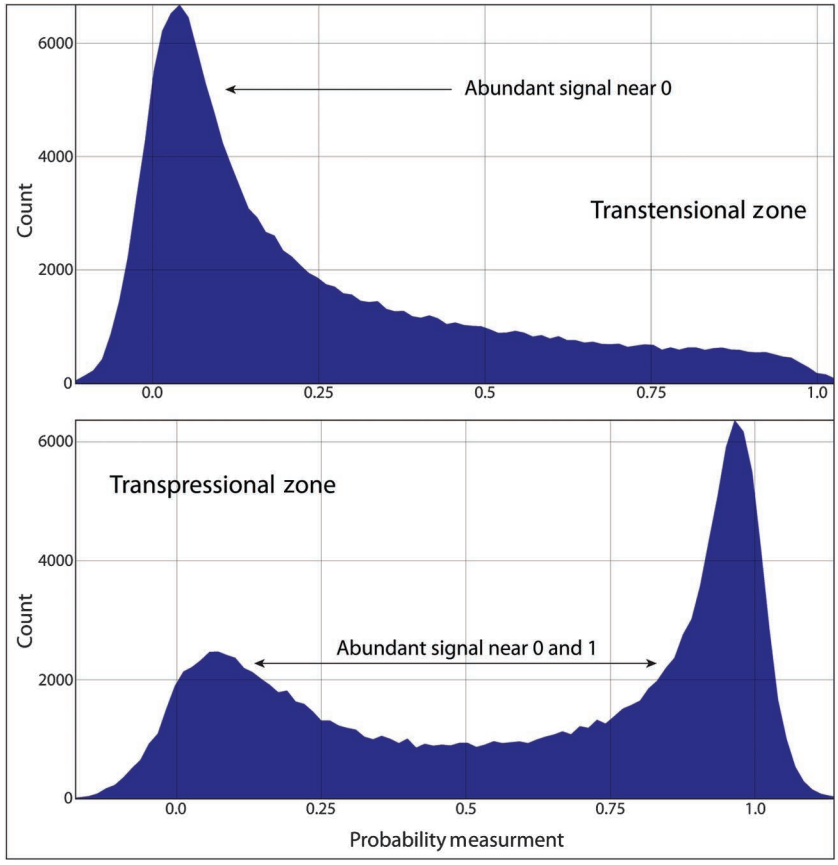

high-resolution seafloor and water column imagery (e.g., Connolly, 2015).

Future work will hopefully include the collection and interpretation of seafloor multibeam and water column backscatter data across the 3D seismic survey area. Integration of the seismic attribute results with high-resolution seafloor and water column backscatter information may provide a link between surface and subsurface processes, such as substrate fluid migration and seabed fluid expulsion (e.g., Berndt, 2005; Ligtenberg, 2005; Judd and Hovland, 2007; Gay et al., 2012; Kluesner et al., 2013; Brothers et al., 2014). Furthermore, the integration of surface and water-column data sets with 3D seismic data could provide a more robust analysis and evaluation of the accuracy of the 3D seismic attribute results.

Conclusion

In this study, we present a poststack data conditioning and neural-network attribute workflow for the detection of faults and potential fluid-pathways in a high-resolution 3D P-Cable seismic volume collected across the HFZ. Structural calculations and structural filtering improved data quality by removing noise predominantly orientated in the inline and crossline directions. Following data conditioning, a neural-network fault attribute workflow has helped to delineate a complicated network of faults. Our results provided better noise tolerance and suppression of unwanted seismic discontinuities relative to single discontinuity attribute approaches. Application of a neural-network chimney attribute workflow provided additional insight into probable fluid pathways through the 3D seismic volume. Visualizing the fault and chimney neural-network attribute results using transparency color schemes allowed for enhanced visual interpretation of the relationship between faulting and probable fluid pathways.

Combining the maximum curvature attribute and structural interpretations with the neural-network attribute results provided additional insight, revealing a strong relationship between deformation associated with strike-slip fault kinematics and the distribution of probable fluid pathways. Our results suggest that transtension, subsidence, and formation of small sedimentary basins result in focused fluid migration along discreet faults. In contrast, transpressional deformation along restraining bends and fault-convergence zones leads to the formation of structurally controlled traps, localized reservoirs, and distributed updip fluid migration. Strike-slip fault strands associated with these transpressional zones cut through the structural traps, providing leakage pathways toward the seafloor. It is likely that other strike-slip faults offshore California are characterized by similar relationships between fault kinematics and fluid migration.

Acknowledgments

We thank PG&E for publicly releasing the 3D seismic data volume as part of the Central Coastal California Seismic Imaging Project. We also thank S. Nishenko, G. Greene, and P. Hogan. We are grateful to OpendTect and dGB Earth Sciences for the use of their software and associated plug-ins. S. Johnson and J. Watt provided very helpful and insightful discussions on the HFZ and its associated geologic background. We thank D. Ebuna for a helpful review and for providing additional details on the acquisition of the 3D P-cable data. In addition, P. Hart is thanked for a constructive review. Any use of trade, firm, or product names is for descriptive purposes only and does not imply endorsement by the U.S. government.

References

Al-Dossary, S., and K. J. Marfurt, 2006, 3D volumetric multispectral estimates of reflector curvature and rotation: Geophysics, **71**, no. 5, P41–P51, doi: 10.1190/1.2242449.

Aminzadeh, F., and P. F. M. de Groot, 2004, Soft computing for qualitative and quantitative seismic object and reservoir property prediction. Part 1: Neural network applications: First Break, **22**, 49–54.

Aminzadeh, F., and P. F. M. de Groot, 2005, A neural network based seismic object detection technique: 85th Annual International Meeting, SEG, Expanded Abstracts, 775–778, doi: 10.1190/1.2144442.

Aminzadeh, F., and P. F. M. de Groot, 2006, Neural networks and other soft computing techniques with applications in the oil industry: EAGE Publications B.V.

Bahorich, M. S., and S. L. Farmer, 1995, 3-D seismic discontinuity for faults and stratigraphic features: The coherence cube: The Leading Edge, **14**, 1053–1058, doi: 10.1190/1.1437077.

Berndt, C., 2005, Focused fluid flow in passive continental margins: Philosophical Transactions of the Royal Society of London A: Mathematical, Physical and Engineering Sciences, **363**, 2855–2871, doi: 10.1098/rsta.2005.1666.

Brookshire, B., and L. Scott, 2015, Reducing risk in offshore planning and development: GEO ExPro Magazine, **12**, 72–74.

Brothers, D. S., C. Ruppel, J. W. Kluesner, U. S. ten Brink, J. D. Chaytor, J. C. Hill, B. D. Andrews, and C. Flores, 2014, Seabed fluid expulsion along upper slope and outer shelf of the U.S. Atlantic continental margin: Geophysical Research Letters, **41**, 96–101, doi: 10.1002/2013GL058048.

Brouwer, F. C. G., D. Connolly, and K. M. Tingahl, 2011, A guide to the practical use of neural networks: 31st Annual Gulf Coast Section Society of Sedimentary Geology, 440–472.

Brouwer, F. C. G., and A. Huck, 2011, An integrated workflow to optimize discontinuity attributes for the imaging of faults: 31st Annual Gulf Coast Section Conference Society of Sedimentary Geology, 496–532.

Chopra, S., and K. J. Marfurt, 2005, Seismic attributes — A historical perspective: Geophysics, **70**, no. 5, 3SO–28SO, doi: 10.1190/1.2098670.

Chopra, S., and K. J. Marfurt, 2007, Seismic attributes for prospect identification and reservoir characterization: SEG.

Chopra, S., and K. J. Marfurt, 2009, Detecting stratigraphic features via crossplotting of seismic discontinuity attributes and their volume visualization: The Leading Edge, **28**, 1422–1426, doi: 10.1190/1.3272695.

Chopra, S., and K. J. Marfurt, 2010, Integration of coherence and volumetric curvature images: The Leading Edge, **29**, 1092–1107, doi: 10.1190/1.3485770.

Connolly, D. L., 2015, Visualization of vertical hydrocarbon migration in seismic data: Case studies from the Dutch North Sea: Interpretation, **3**, SX21–SX27, doi: 10.1190/INT-2015-0007.1.

Connolly, D. L., and R. Garcia, 2012, Tracking hydrocarbon seepage in Argentina's Neuquen basin: World Oil, July 2012, 101–104.

Dickinson, W. R., M. Ducea, L. I. Rosenberg, G. H. Greene, S. A. Graham, J. C. Clark, G. E. Weber, S. Kiddler, W. G. Ernst, and E. E. Brabb, 2005, Net dextral slip, Neogene San Gregorio-Hosgri Fault Zone, coastal California: Geological evidence and tectonic implications: Geological Society and America Special Paper 391, 1–43.

Dupré, S., C. Scalabrin, C. Grall, J. Augustin, P. Henry, A. M. Şengör, N. Görü, M. Çağatay, and L. Géli, 2015, Tectonic and sedimentary controls on widespread gas emissions in the Sea of Marmara: Results from systematic, shipborne multibeam echo sounder water column imaging: Journal of Geophysical Research: Solid Earth, **120**, 2891–2912, doi: 10.1002/2014JB011617.

Ebuna, D. R., T. J. Mitchell, P. J. Hogan, S. Nishenko, and H. G. Greene, 2013, High-resolution offshore 3D seismic geophysical studies of infrastructure geohazards: 26th Symposium on the Application of Geophysics to Engineering and Environmental Problems, 311–320.

Fugro Consultants Inc., 2012, Software validation of Uniseis and 3D data qualification of 2010–2011 high-resolution marine survey data, Offshore Diablo Canyon Power Plant, Central Coastal California Seismic Imaging Project: Report No. PGEQ-PR-03 (Rev0), FSI Project No. 2011-4493, 1–67.

Gay, A., R. Mourgues, C. Berndt, D. Bureau, S. Planke, D. Laurent, S. Gautier, C. Lauer, and D. Loggia, 2012, Anatomy of a fluid pipe in the Norway Basin: Initiation, propagation and 3D shape: Marine Geology, **332**, 75–88, doi: 10.1016/j.margeo.2012.08.010.

Gersztenkorn, A., and K. J. Marfurt, 1999, Eigenstructure-based coherence computations as an aid to 3-D structural and stratigraphic mapping: Geophysics, **64**, 1468–1479, doi: 10.1190/1.1444651.

Hansen, K. L., W. R. Letis, M. K. McLaren, W. U. Savage, and N. T. Hall, 2004, Style and rate of Quaternary deformation of the Hosgri Fault Zone, offshore south-central California: U.S. Geological Survey Bulletin 1995-BB, 1–33.

Heggland, R., 2005, Using gas chimney in seal integrity analysis: A discussion based on case histories, *in* P. Boult, and J. Kaldi, eds., Evaluating fault and cap rock seals: AAPG Hedberg Series, 237–245.

Hein, J. R, W. R. Normark, B. R. McIntyre, T. D. Lorenson, and C. L. Powell, 2006, Methanogenic calcite, 13C-depleted bivalve shells, and gas hydrate from a mud volcano offshore southern California: Geology, **34**, 109–112, doi: 10.1130/G22098.1.

Isaacs, C. M., K. A. Pisciotto, and R. E. Garrison, 1983, Facies and diagenesis of the Miocene Monterey Formation, California: A summary: Developments in Sedimentology, **36**, 247–282, doi: 10.1016/S0070-4571(08)70094-3.

Johnson, S. Y., S. R. Hartwell, and P. Dartnell, 2014, Offset of latest Pleistocene shoreface reveals slip rate on the Hosgri strike-slip fault, offshore Central California: Bulletin of the Seismological Society of America, **104**, 1650–1662, doi: 10.1785/0120130257.

Johnson, S. Y., and J. T. Watt, 2012, Influence of fault trend, bends, and convergence on shallow structure and geomorphology of the Hosgri strike-slip fault, offshore central California: Geosphere, **8**, 1632–1656, doi: 10.1130/GES00830.1.

Judd, A., and M. Hovland, 2007, Seabed fluid flow: The impact on geology biology and the marine environment: Cambridge University Press.

Kluesner, J. W., E. Silver, S. Nale, N. Bangs, and K. McIntosh, 2013, Fluid migration along a dense, intersecting array of faults on the outer-shelf of Southern Costa Rica: Insights from 3D seismic attributes and multibeam data: Mineralogical Magazine, **77**, 1480, doi: 10.1180/minmag.2013.077.5.11.

Lettis, W. R., K. L. Hansen, J. R. Unruh, M. K. McLaren, and W. U. Savage, 2004, Quaternary tectonic setting of south-central coastal California: U.S. Geological Survey Bulletin 1995-AA.

Ligtenberg, J. H., 2005, Detection of fluid migration pathways in seismic data: Implications for fault seal analysis: Basin Research, **17**, 141–153, doi: 10.1111/j.1365-2117.2005.00258.x.

Løseth, H., M. Gading, and L. Wensaas, 2009, Hydrocarbon leakage interpreted on seismic data: Marine and Petroleum Geology, **26**, 1304–1319, doi: 10.1016/j.marpetgeo.2008.09.008.

Maloney, J. M., B. M. Grupe, A. L. Pasulka, K. S. Dawson, D. H. Case, C. A. Frieder, L. A. Levin, and N. W. Driscoll, 2015, Transpressional segment boundaries in strike-slip fault systems offshore southern California: Implications for fluid expulsion and cold seep habitats: Geophysical Research Letters, **42**, 4080–4088, doi: 10.1002/2015GL063778.

Mann, P., 2007, Global catalogue, classification and tectonic origins of restraining- and releasing bends on active and ancient strike-slip fault systems: Geological

Society of London, Special Publications, **290**, 13–142, doi: 10.1144/SP290.2.

Marfurt, K. J., 2014, Seismic attributes and the road ahead: 84th Annual International Meeting, SEG, Expanded Abstracts, 4421–4425, doi: 10.1190/segam2014-1644.1.

Marfurt, K. J., 2015, Techniques and best practices in multiattribute display: Interpretation, **3**, B1–B23, doi: 10.1190/INT-2014-0133.1.

Marfurt, K. J., and T. M. Alves, 2014, Pitfalls and limitations in seismic attribute interpretation of tectonic features: Interpretation, **3**, SB5–SB15, doi: 10.1190/INT-2014-0122.1.

Marfurt, K. J., R. L. Kirlin, S. L. Farmer, and M. S. Bahorich, 1998, 3-D seismic attributes using a semblance-based coherency algorithm: Geophysics, **63**, 1150–1165, doi: 10.1190/1.1444415.

Marfurt, K. J., V. Sudhaker, A. Gersztenkorn, K. D. Crawford, and S. E. Nissen, 1999, Coherency calculations in the presence of structural dip: Geophysics, **64**, 104–111, doi: 10.1190/1.1444508.

McCaffrey, R., 2005, Block kinematics of the Pacific-North America plate boundary in the southwestern United States from inversion of GPS, seismological, and geologic data: Journal of Geophysical Research: Solid Earth, **110**, 1–27, doi: 10.1029/2004JB003307.

Meade, B. J., and B. H. Hager, 2005, Block models of crustal motion in southern California constrained by GPS measurements: Journal of Geophysical Research: Solid Earth, **110**, 1–19, doi: 10.1029/2004JB003209.

Means, W. D., 2012, Stress and strain: Basic concepts of continuum mechanics for geologists: Springer Science & Business Media, 1–339.

Meldahl, P., R. Heggland, B. Bril, and P. F. M. de Groot, 1999, The chimney cube, an example of semi-automated detection of seismic objects by directive attributes and neural networks. Part 1: Methodology: 79th Annual International Meeting, SEG, Expanded Abstracts, 931–934, doi: 10.1190/1.1821262.

Meldahl, P., R. Heggland, B. Bril, and P. F. M. de Groot, 2001, Identifying fault and gas chimneys using multiattributes and neural networks: The Leading Edge, **20**, 474–482, doi: 10.1190/1.1438976.

Mirkamali, M. S., N. Keshavarz Fk, and M. R. Bakhtiari, 2013, Fault zone identification in the eastern part of the Persian Gulf based on combined seismic attributes: Journal of Geophysics and Engineering, **10**, 1–11, doi: 10.1088/1742-2132/10/1/015007.

Nishenko, S., P. Hogan, and R. Kvitek, 2012, Seafloor mapping for earthquake, tsunami hazard assessments: Sea Technology, **53**, 15–20.

Ohl, D., and A. Raef, 2014, Rock formation characterization for carbon dioxide geosequestration: 3D seismic amplitude and coherency anomalies, and seismic petrophysical facies classification, Wellington and Anson-Bates Fields, Kansas, USA: Journal of Applied Geophysics, **103**, 221–231, doi: 10.1016/j.jappgeo.2014.01.017.

Pacific Gas and Electric Company (PG&E), 2014, Offshore low-energy seismic reflection studies in Estero Bay, San Luis Obispo Bay, and Point Sal Areas: PG&E Technical Report, GEO.DCPP.TR.14.02, http://www.pge.com/includes/docs/pdfs/safety/systemworks/dcpp/report/Ch3.GEO.DCPP.TR.14.02_R0_txt.w.ITR.pdf.

Paull, C. K., W. R. Normark, W. Ussler, D. W. Caress, and R. Keaton, 2008, Association among active seafloor deformation, mound formation, and gas hydrate growth and accumulation within the seafloor of the Santa Monica Basin, offshore California: Marine Geology, **250**, 258–275, doi: 10.1016/j.margeo.2008.01.011.

Petersen, C. J., S. Bünz, S. Hustoft, J. Mienert, and D. Klaeschen, 2010, High-resolution P-Cable 3D seismic imaging of gas chimney structures in gas hydrated sediments of an Arctic sediment drift: Marine and Petroleum Geology, **27**, 1981–1994, doi: 10.1016/j.marpetgeo.2010.06.006.

Pisciotto, K. A., and R. E. Garrison, 1981, Lithofacies and depositional environments of the Monterey Formation, California, *in* R. E. Garrison, R. G. Douglas, K. E. Pisciotto, C. M. Isaacs, and J. C. Ingle, eds., The Monterey Formation and related siliceous rocks of California: Pacific Section of the Society of Economic Paleontologists Mineralogists Symposium Special Publication, 97–122.

Roberts, A., 2001, Curvature attributes and their application to 3D interpreted horizons: First Break, **19**, 85–100, doi: 10.1046/j.0263-5046.2001.00142.x.

Russell, B., D. Hampson, J. Schuelke, and J. Quirein, 1997, Multiattribute seismic analysis: The Leading Edge, **16**, 1439–1444, doi: 10.1190/1.1437486.

Sorlien, C. C., M. J. Kamerling, and D. Mayerson, 1999, Block rotation and termination of the Hosgri strike-slip fault, California, from three-dimensional map restoration: Geology, **27**, 1039–1042, doi: 10.1130/0091-7613(1999)027<1039:BRATOT>2.3.CO;2.

Tingdahl, K. M., 1999, Improving seismic detectability using intrinsic directionality: M.S. thesis, Earth Sciences Centre, Göteborg University, paper no. B194.

Tingdahl, K. M., Ø. Steen, P. Meldahl, and J. H. Ligtenberg, 2001, Semi-automatic detection of faults in 3-D seismic signals: 81st Annual International Meeting, SEG, Expanded Abstracts, 1953–1956, doi: 10.1190/1.1816520.

Tingdahl, K. M., and P. F. M. de Groot, 2003, Poststack dip and azimuth processing: Journal of Seismic Exploration, **12**, 113–126.

Tingdahl, K. M., and M. de Rooij, 2005, Semi-automatic detection of faults in 3D seismic data: Geophysical Prospecting, **53**, 533–542, doi: 10.1111/j.1365-2478.2005.00489.x.

Titus, S. J., M. Dyson, C. DeMets, B. Tikoff, F. Rolandone, and R. Bürgmann, 2011, Geologic versus geodetic deformation adjacent to the San Andreas fault, central California: Geological Society of America Bulletin, **123**, 794–820, doi: 10.1130/B30150.1.

Jared Kluesner received a B.S. (2006) from Indiana State University and a Ph.D. (2011) from Scripps Institution of Oceanography. In 2012, he became a postdoctoral scholar at the University of California Santa Cruz (UCSC), where he conducted research on the geophysical detection and visualization of faults and fluid-migration pathways along the Costa Rican margin. In 2014, he became a researcher at UCSC and led a cooperative project with the USGS Florida Water Science Center studying karst structures aquifer systems using 2D/3D seismic data and seismic attribute analysis. In 2015, he joined the USGS Pacific Coastal and Marine Science Center in Santa Cruz, California. His current research interests include swath sonar and 2D/3D seismic reflection acquisition, processing, and visualization techniques.

Danny Brothers received a B.A. (2004) from the University of Colorado, Boulder, and a Ph.D. (2009) from the Scripps Institution of Oceanography. He then moved to Woods Hole, MA, to work as a Mendenhall Postdoc Fellow, which started his career at the USGS. He is a research geophysicist at the USGS in Santa Cruz, California. His research is primarily focused on two elements: (1) understanding the tectonics, sedimentary processes, and morphological evolution of continental margins and (2) the development of new approaches to quantify submarine earthquake, landslide, and tsunami hazards in U.S. territory. His research involves a significant amount of seagoing geophysical fieldwork, mostly in the form of high-resolution seismic reflection and swath bathymetry methods.